Determination of water depth with high-resolution satellite imagery over variable bottom types

Richard P. Stumpf[1] *and Kristine Holderied*

NOAA National Ocean Service, Center for Coastal Monitoring and Assessment, 1305 East–West Highway rm 9115, Silver Spring, Maryland 20910

Mark Sinclair

Tenix LADS Corporation, Mawson Park, South Australia, 5095, Australia

Abstract

A standard algorithm for determining depth in clear water from passive sensors exists; but it requires tuning of five parameters and does not retrieve depths where the bottom has an extremely low albedo. To address these issues, we developed an empirical solution using a ratio of reflectances that has only two tunable parameters and can be applied to low-albedo features. The two algorithms—the standard linear transform and the new ratio transform—were compared through analysis of IKONOS satellite imagery against lidar bathymetry. The coefficients for the ratio algorithm were tuned manually to a few depths from a nautical chart, yet performed as well as the linear algorithm tuned using multiple linear regression against the lidar. Both algorithms compensate for variable bottom type and albedo (sand, pavement, algae, coral) and retrieve bathymetry in water depths of less than 10–15 m. However, the linear transform does not distinguish depths >15 m and is more subject to variability across the studied atolls. The ratio transform can, in clear water, retrieve depths in >25 m of water and shows greater stability between different areas. It also performs slightly better in scattering turbidity than the linear transform. The ratio algorithm is somewhat noisier and cannot always adequately resolve fine morphology (structures smaller than 4–5 pixels) in water depths >15–20 m. In general, the ratio transform is more robust than the linear transform.

Since the first use of aerial photography over clear shallow water, it has been recognized that water depth can be estimated in some way by remote sensing. The theory developed by Lyzenga (1978, 1981) and expanded by Philpot (1989) and Maritorena et al. (1994) demonstrated the validity of, and problems involved with, using passive remote sensing for determination of water depth. The use of two or more bands allows separation of variations in depth from variations in bottom albedo, but compensation for turbidity, while tractable, can be problematic. Although passive optical systems are limited in depth penetration and constrained by water turbidity, the use of such satellite data might be the only viable way to characterize either extensive or remote coral reef environments. Besides the obvious need for bathymetric information in many remote areas, mapping of coral reefs and characterization of potential for bleaching requires information on water depth. Coral reefs, by their nature, strongly influence the physical structure of their environment, and water depth information is fundamental to discriminating and characterizing coral reef habitat, such as patch reef, spur-and-groove, and seagrass beds. Knowledge of water depth also allows estimation of bottom albedo, which can improve habitat mapping (Mumby et al. 1998). Knowledge of the detailed structure of the bottom helps in characterizing the role and quality of the reef as a fish environment. However, extensive areas of coral reefs in the ocean have little, incomplete, or spatially limited data on bathymetry because of the difficulty obtaining accurate and well-distributed soundings in remote reef areas. A robust method of estimating bathymetry directly from the passive satellite imagery would enhance our capability to map these regions.

In order to map coral reef environments, high spatial resolution is required because of the relatively small horizontal spatial scales and the ecological importance of vertical structures in those environments in the form of patch reefs, spur-and-groove, mini-atolls, and so on. Mapping the fine-scale variability will improve characterization of habitat, both for corals and for various species living in the reefs. Until recently, only two options existed for such information: airborne measurements (photo and hyperspectral) and multispectral satellite imagery (typically Landsat). Although aircraft can provide high-resolution data, either spatially or spectrally, high costs and deployment issues limit their use for comprehensive regional mapping in remote areas. Landsat, particularly the Landsat-7 enhanced thematic mapper (ETM), offers global coverage of coral reefs, but only with a 30-m field of view. With the launch of high-resolution sensors IKONOS in 1999 and QuickBird in 2002, 4-m (or better) field-of-view multispectral imagery became available from space, providing a new resource for the development of mapping and monitoring programs for coral reefs in remote locations. These systems provide multispectral data with three visible bands (blue, green, red), which can simulate aerial photography, and one near-infrared (near-IR) band. This study focuses on IKONOS imagery; however, the

---

Table 1. Spectral bands for IKONOS, with Landsat-7 ETM for comparison.

| Spectral region | Spectral bands (nm) | |
	IKONOS	Landsat-7
Blue	445–515	450–520
Green	510–595	530–610
Red	630–700	630–690
Near-infrared	760–850	780–900

same depth estimation methods can be applied to Landsat imagery because of the similarity in the spectral bands (Table 1).

The standard bathymetry algorithm has a theoretical derivation (Lyzenga 1978) but also incorporates empirical tuning as an inherent part of the depth estimation process. It is preferable to minimize such tuning, particularly for remote regions where benthic and water quality parameters can be hard to measure or estimate. This paper examines an alternative bathymetry algorithm and addresses two basic problems in the application of bathymetry algorithms to mapping coral reefs: (1) the stability of an algorithm with fixed coefficients within and between atolls and (2) the behavior of the algorithms in describing relative and absolute depths at various scales.

Materials and methods

Study area—The area under investigation in this paper includes two coral reef atolls in the northwest Hawaiian Islands. This island chain extends over 1,800 km of the north Pacific from Nihoa Island at 162°W to Kure Atoll at 178.5°W. The area encompasses two National Wildlife Refuges, a Hawaiian State Wildlife Sanctuary, and the new U.S. Northwestern Hawaiian Islands Coral Reef Ecosystem Reserve, which is proposed for designation as a U.S. National Marine Sanctuary. There are 10 emergent atolls and reefs and several shallow banks. The reef and bank areas include >7,000 km² of area less than 25 fathoms (45 m) in depth (the absolute maximum depth detectable by passive remote sensing and a boundary demarcation for some regulated activities within the Reserve), making it the largest shallow-water coral reef area under direct U.S. jurisdiction. The area is remote, and the two atolls discussed here, Kure Atoll and Pearl and Hermes Reef (henceforth called Pearl), are located nearly 2,000 km from Honolulu. The shallow-water environments of these two atolls are considerable in area, with 100 km² at Kure and 500 km² at Pearl. Kure Atoll was home to a U.S. Coast Guard Loran station and has accurate soundings within the lagoon, but few or no soundings in the fore-reef area. In addition, outside of a narrow corridor to the main island, many of the Kure reefs are not mapped in sufficient detail to assure confidence in navigation. Even with these limitations, Kure has more depth information than Pearl, where one third of the lagoon has no bathymetric information at all, and the charts show only the general form of the maze of mini-atolls and extensive lines of reticulated reefs within the lagoon.

The atolls have substrates varying from sand to pavement to live coral, with cover that includes various densities of algae and smaller corals. The sand is usually coralline and white with an extremely high albedo in higher energy areas. With an increasing proportion of coral gravel and rubble, the sediments tend to have a tan or brown appearance. Pavement is typically gray to olive brown in appearance, varies from low to high rugosity, and is often covered with varying densities of algae. In areas where coral is found at high density at Kure and Pearl, *Porites compressa* (finger coral) is the most common species, with other dominant corals including *Montipora capitata* (rice coral), *Porites lobata* (lobe coral), *Montipora flabellata* (blue rice coral), and *Pocillopora meandrina* (cauliflower coral). Algal cover includes varieties of red, brown, and green macroalgae, as well as filamentous turf algae. The reef flats are typically dominated by encrusting coralline algae, with some green algae (e.g., *Halimeda* sp.).

Model—The depth estimation method uses the reflectances for each satellite imagery band, calculated with the sensor calibration files and corrected for atmospheric effects. The reflectance of the water, R_w, which includes the bottom where the water is optically shallow, is defined as

$$R_w = \frac{\pi L_w(\lambda)}{E_d(\lambda)} \qquad (1)$$

where L_w is the water-leaving radiance, E_d is the downwelling irradiance entering the water, and λ is the spectral band. L_w and R_w refer to values above the water surface. R_w is found by correcting the total reflectance R_T for the aerosol and surface reflectance, as estimated by the near-IR band, and for the Rayleigh reflectance R_r (Eq. 2).

$$R_w = R_T(\lambda_i) - Y(\lambda_i)R_T(\lambda_{IR}) - R_r(\lambda_i) \qquad (2)$$

Y is the constant to correct for spectral variation (equivalent to the Angstrom exponent in Gordon et al. [1983]), subscript i denotes a visible channel, and subscript IR denotes the near-IR channel. R_T is found from Eq. 3.

$$R_T(\lambda_i) = \frac{\pi L_T(\lambda_i)/E_0(\lambda_i)}{(1/r^2)T_0(\lambda_i)T_1(\lambda_i)\cos\,\theta_0} \qquad (3)$$

L_T is the (total) radiance measured at the satellite, E_0 is the solar constant, r is the earth–sun distance in astronomical units, θ_0 is the solar zenith angle, and T_0 and T_1 are the transmission coefficients for sun-to-earth and earth-to-satellite, respectively.

The atmospheric correction is based on the algorithm developed by Gordon et al. (1983) for the Coastal Zone Color Scanner (CZCS) and by Stumpf and Pennock (1989) for the Advanced Very High Resolution Radiometer (AVHRR) and is similar to that recommended for Landsat (Chavez 1996; Zhang et al. 1999). The Y coefficient in Eq. 2 depends on aerosol type. For IKONOS, the correction presumes a maritime atmosphere with a spectral variation similar to that of the water surface specular reflectance. This proves to be a reasonable assumption here; however, separation of the aerosol correction (with a scale of hundreds of meters) from the specular surface reflectance correction (with a scale of tens

of meters) might be required for more generic use of IKO-NOS data. Although IKONOS does not have onboard calibration, postlaunch calibrations have been established by the commercial vendor, Space Imaging. Additional comparisons with Landsat-7, which does have onboard calibration, as well as the sea-viewing wide field-of-view sensor (SeaWiFS), might aid in calibration for future work. Residual miscalibration will result in alteration of the atmospheric model of choice and, to a lesser degree, in the empirical coefficients chosen for the depth estimation algorithms.

Bathymetry—Linear transform: Light is attenuated exponentially with depth in the water column, with the change expressed by Beer's Law (Eq. 4).

$$L(z) = L(0)\exp(-Kz) \qquad (4)$$

K is the attenuation coefficient and z is the depth. Any analysis of light with depth must take into account this exponential decrease in radiance with depth. Lyzenga (1978) showed that the relationship of observed reflectance (or radiance) to depth and bottom albedo could be described as

$$R_w = (A_d - R_\infty)\exp(-gz) + R_\infty \qquad (5)$$

where R_∞ is the water column reflectance if the water were optically deep, A_d is the bottom albedo, z is the depth, and g is a function of the diffuse attenuation coefficients for both downwelling and upwelling light. Equation 5 can be rearranged to describe the depth in terms of the reflectances and the albedo (Eq. 6).

$$z = g^{-1}[\ln(A_d - R_\infty) - \ln(R_w - R_\infty)] \qquad (6)$$

The estimation of depth from a single band using Eq. 6 will depend on the albedo A_d, with a decrease in albedo resulting in an increase in the estimated depth. Lyzenga (1978, 1985) showed that two bands could provide a correction for albedo in finding the depth and created from Eq. 6 the linear solution in Eq. 7.

$$Z = a_0 + a_i X_i + a_j X_j \qquad (7)$$

where

$$X_i = \ln[R_w(\lambda_i) - R_\infty(\lambda_i)] \qquad (8)$$

The constants a_0, a_i, and a_j usually are determined from multiple linear regression (or a similar technique). For any solution for depth from passive systems, variations in water clarity and spectral variation in absorption pose additional complications (Philpot 1989; Van Hengel and Spitzer 1991). The linear transform solution above has five variables that must be determined empirically: $R_\infty(\lambda_i)$, $R_\infty(\lambda_j)$, a_0, a_i, and a_j. Having to adjust five empirical coefficients can be problematic for large areas, even with relatively small variations in water quality conditions. In addition, when the bottom albedo is low, as can occur with dense macroalgae or seagrass, then A_d is less than R_∞. As a result, the depth cannot be found without using an entirely new algorithm, because X is undefined if $(R_w - R_\infty)$ is negative (logarithm of a negative number).

Ratio transform: The problem of mapping shallow-water areas with significantly lower reflectance than adjacent, op-
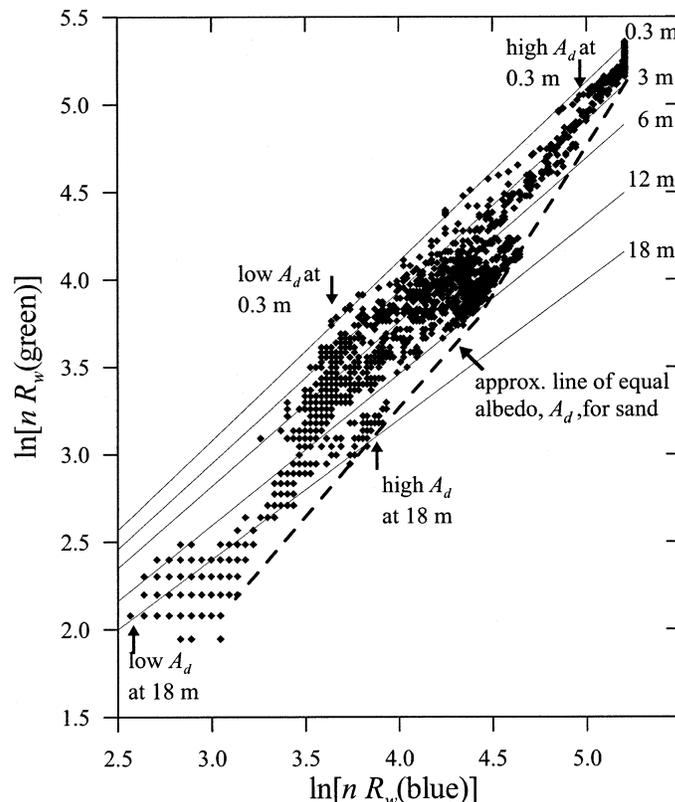

Fig. 1. Log transformation used for ratio algorithm with data from Kure Atoll. The lines of constant depth are also lines of fixed ratio (0.3 m is also the blue to green ratio of 0.975; 18 m is a ratio of 1.251). Depths were assigned to the constant ratio lines using the tuning described in this paper. The dashed line shows the approximate values for a sand bottom that has the same albedo at all depths. The attenuation of light with depth means that features have lower R_w in deeper water, regardless of their intrinsic albedo. A decrease in albedo causes values to move down the lines of constant ratio. "High A_d" indicates carbonate sand of nominally similar albedo at both 0.3 and 18 m. "Low A_d" indicates similar albedo over dense algal cover at both depths.

tically deep waters provided the initial motivation to develop an alternative algorithm. Because we are interested in mapping relatively large and remote coral reef areas, we also searched for an alternative solution that has fewer parameters, thereby requiring less empirical tuning and having the potential of being more robust over variable bottom habitats.

With bands having different water absorptions, one band will have arithmetically lesser values than the other. Accordingly, as the log values change with depth, the ratio will change (Fig. 1). As the depth increases, while the reflectance of both bands decreases, $\ln(R_w)$ of the band with higher absorption (green) will decrease proportionately faster than $\ln(R_w)$ of the band with lower absorption (blue). Accordingly, the ratio of the blue to the green will increase. A ratio transform will also compensate implicitly for variable bottom type. A change in bottom albedo affects both bands similarly (cf. Philpot 1989), but changes in depth affect the high absorption band more. Accordingly, the change in ratio because of depth is much greater than that caused by change
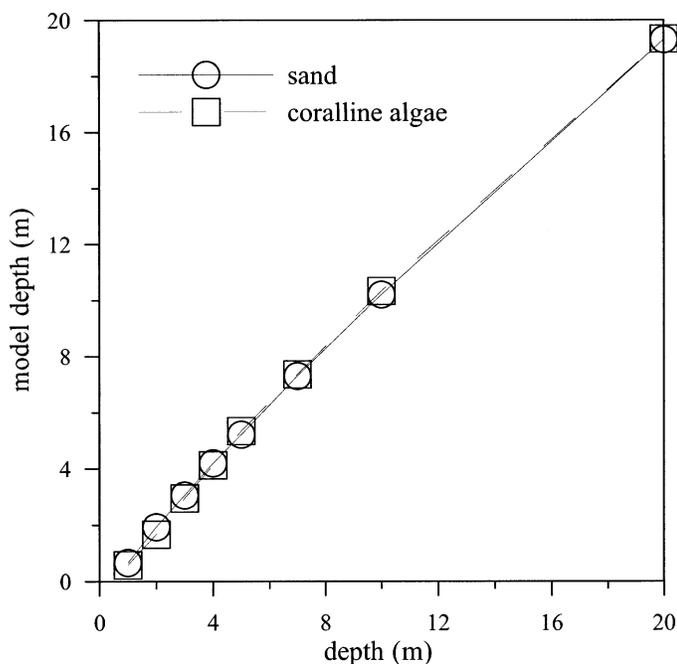
Fig. 2. Depths determined from the top-of-atmosphere radiances modeled by Lubin et al. (2001). *X*-axis shows depths input into the Lubin et al. (2001) model. *Y*-axis shows depths retrieved from the ratio algorithm using Lubin's modeled radiances and Eqs. 1–3 and 9 from this paper.

in bottom albedo, suggesting that different bottom albedoes at a constant depth will still have the same ratio (Fig. 1). If this ratio condition applies, we would expect that the ratio would approximate depth independently of bottom albedo and need only be scaled to the actual depth; namely,

$$Z = m_1 \frac{\ln(nR_w(\lambda_i))}{\ln(nR_w(\lambda_j))} - m_0 \qquad (9)$$

where m_1 is a tunable constant to scale the ratio to depth, n is a fixed constant for all areas, and m_0 is the offset for a depth of 0 m ($Z = 0$), analogous to a_0 in Eq. 7. The fixed value of n in Eq. 9 is chosen to assure both that the logarithm will be positive under any condition and that the ratio will produce a linear response with depth.

The ratio algorithm was examined against the model results of Lubin et al (2001) to evaluate the empirical solution. Lubin et al. (2001) created simulated top-of-atmosphere radiances for Landsat bands 1 and 2 for different bottom types. These radiances were reduced to water reflectances using Eqs. 1–3, then Eq. 9 was used to estimate the depth (Fig. 2). Two bottom types from Lubin et al. (2001) with different bottom albedos were examined: sand ($A_d = 41\%$ at 500 nm) and coralline algae ($A_d = 17\%$ at 500 nm). A single set of coefficients, m_1 and m_0, were optimized to minimize error for both bottom types. The root mean square (rms) error was < 0.4 m between the input model depths and our estimated depths to 20 m. The result indicates that the ratio algorithm has the potential to be effective. The model analysis further indicates that the depth calculation is insensitive (rms error < 0.4 m) to threefold changes in the value of n (n varying from 500 to 1,500).

Although one could construct various empirical algorithms with a variety of band combinations, including reflectances without the log transform, all would require more parameters and more complex tuning than the ratio solution of Eq. 9 (or the linear algorithm for that matter).

Evaluation and development—Satellite data: The IKONOS satellite was launched in September 1999 by the commercial vendor, Space Imaging. The satellite has two sensors: one panchromatic with a 1-m nominal field of view and one multispectral with a 4-m nominal field of view when viewing at nadir. The instrument is a pushbroom sensor that collects an 11-km swath up to 1,000 km in length. Multiple (shorter) swaths of an area can be collected on the same orbit because the satellite has a pointing capability. The panchromatic sensor observes light from the green to the near-IR and provides information to a depth of approximately 6 m. The multispectral sensor has four bands, spectrally similar to Landsat (Table 1), with 11-bit digitization in each band. Instrument nominal sensitivity is about fourfold greater than the Landsat-7 ETM. The imagery can be positioned within 15 m with orbital parameters.

Tuning: The tuning of the linear algorithm followed the technique of Lyzenga (1985). R_∞ was presumed to be R_w in optically deep water. The coefficients in Eq. 7 were determined through multivariate linear regression to all the lidar data between 0 and 12 m for an entire transect (=Kure 2). Originally, we tuned to a greater depth range but found significantly worse results.

The ratio transform was tuned using soundings from the nautical chart for Kure. Positions on the nautical charts for the area are located based on the local astronomic data obtained during surveys in 1961, which can be hundreds of meters different from positions based on the current World Geodetic Survey, 1984 (WGS-84) datum, used for both lidar and IKONOS. To address the datum issue, the chart positions were shifted so that reliable features were located within 20 m of their position in the IKONOS imagery. Coefficients m_1 and m_0 in Eq. 9 were obtained from a comparison of image-derived values with chart depths from the beach, three flat areas of different depths in Kure (3, 8, and 12 m) and one sloping area (at ~16 m). Lidar soundings were not used in the tuning of the ratio algorithm. (The manual tuning to chart soundings was tried also for the linear transform, but the results were inferior to the multiple linear regression and were abandoned.) The resultant coefficients for both methods were then applied to all imagery at both Kure and Pearl.

Lidar: Bathymetry was obtained using the airborne LADS Mk II lidar system along eight transects over Kure and 10 over Pearl. Depths from three of these transects are discussed in detail here. The instrument uses a Nd-YAG laser with a 532-nm wavelength. The scanning laser operates at 900 Hz, and the aircraft ground speed is about 150 knots, resulting in a 4- × 4-m laser spot spacing across a swath of ~200 m. The footprint of the laser at the water surface is about 2.5 m and increases slowly with depth. The green returned laser energy is captured by a green receiver and digitized to provide a depth. The aircraft height is determined by the infra-
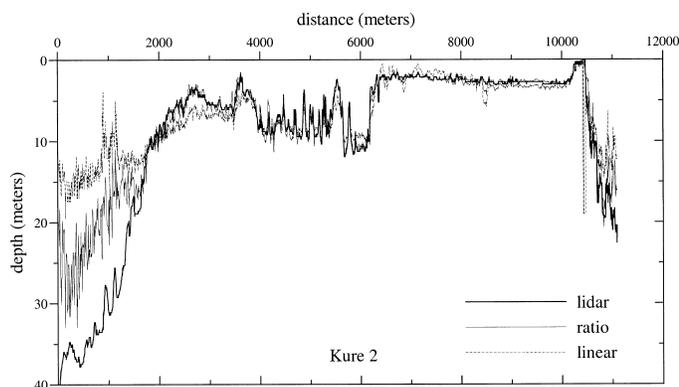
Fig. 3. Profile from Kure Atoll (Kure 2 in text). Distances are in meters from start of lidar line in southwest. Soundings from the nautical chart used for tuning were located in the vicinity of distances 9,000, 3,000, 6,000, and 1,500 m. The depth discrepancy at 1,000 m occurred in a light cloud shadow and should be disregarded; the ratio method does not necessarily perform better under cloud shadows than the linear method.

red laser reflection, which is supplemented by an inertial height reference. The aircraft position was based on Global Positioning System (GPS) measurements by postprocessing against an Ashtech GPS station located at a known reference on Midway Island. Total expected error for horizontal position of a laser sounding was 4 m for this mission. Position of the bottom was determined in an absolute sense against the WGS-84 ellipsoid used for positioning, and the bathymetry was determined by comparing returns from the water surface and the bottom. The maximum water penetration (where a return was reported) in the clearest water in this area exceeded 60 m. The survey met International Hydrographic Standards for accuracy of order 1. Vertical precision of measured relative water depth was <5 cm, as indicated by the crossline comparisons. To determine height relative to mean lower low water, the standard datum for bathymetry, a tidal correction for Midway Island was applied (80 km from Kure and 130 km from Pearl) because tide gauges were not present at either Kure or Pearl. Residual errors from tide uncertainty can be expected to be <15 cm, which is finer than the 30-cm vertical resolution achievable with satellite detection.

Results

The algorithms were examined along three lidar lines; the first of which is an 11-km transect extending across Kure (=Kure 2) from the southwest, a forereef area through the central lagoon to the northeast reef crest, and the forereef (Fig. 3). The central basins were slightly turbid with fine suspended sediment; however the density of this turbidity was insufficient to alter the brightness of the red band, and visibility was typically over 10 m, even in the more turbid areas. A second Kure lidar transect (=Kure 1) of 6 km extends across the northern portion of the atoll from west to east, covering only the forereef and shallow areas along the backreef (Fig. 4). The third transect examined here is a 17-km line running south to north across Pearl (=Pearl 1) and
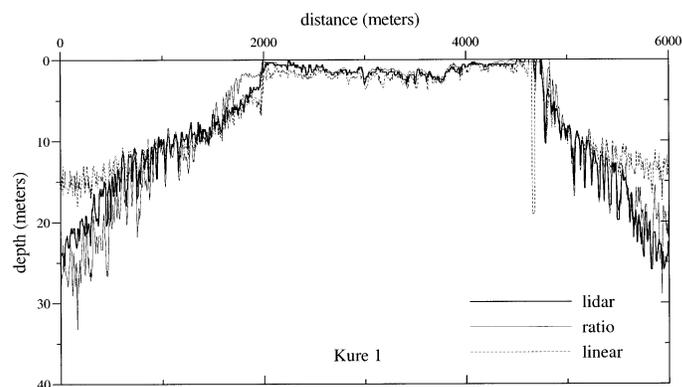

Fig. 4. Profile across forereef (on either side), reef crest, and back reef at Kure Atoll (Kure 1 in text). Depth discrepancies between 1,800 and 2,000 m occur in light cloud shadow.

crossing many steep, reticulated reef structures (Fig. 5). The coefficients tuned to the Kure 2 transect were applied directly to IKONOS imagery from Pearl, without retuning for either the ratio or linear algorithms.

The bathymetry generated by both algorithms is generally effective in mapping depths across both Kure and Pearl, despite distinct differences in the structure of the two atolls, with Kure having a classic atoll lagoon and Pearl having an extensive and complicated reef structure within the lagoon (Fig. 5). Most major vertical features are reproduced (Fig. 6), particularly in shallow water, including shallow basins with sand waves, spur-and-groove on the forereef (Fig. 6A), patch reefs (Fig. 6B), and steep, narrow reticulated reef structures (Fig. 6C,D). Spatial details are also well represented, as can be seen in Fig. 7, which shows an area of Kure with patch reefs in deeper water and sand waves in shallow water. Along the two Kure transects, depths generated with both methods match the lidar data in water less than ~15 m depth. The results from Pearl illustrate a general transferability of the algorithms (Fig. 5), since both methods give meaningful results (to ~15 m) without retuning. Both algorithms also quite effectively recover the steep depth variability over the complex mini-atolls and reticulated reefs of Pearl, including the small depth increase characteristic of the normally sandy center of mini-atolls. However, in relatively
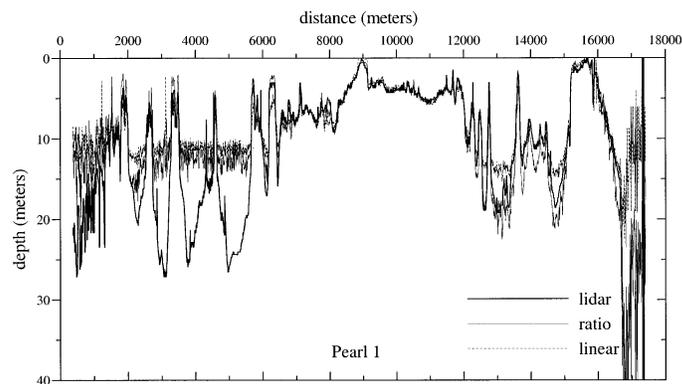

Fig. 5. Profile from Pearl and Hermes Atoll (Pearl 1 in text), crossing patch reefs, mini-atolls, and reef-crest (at 16,000 m).
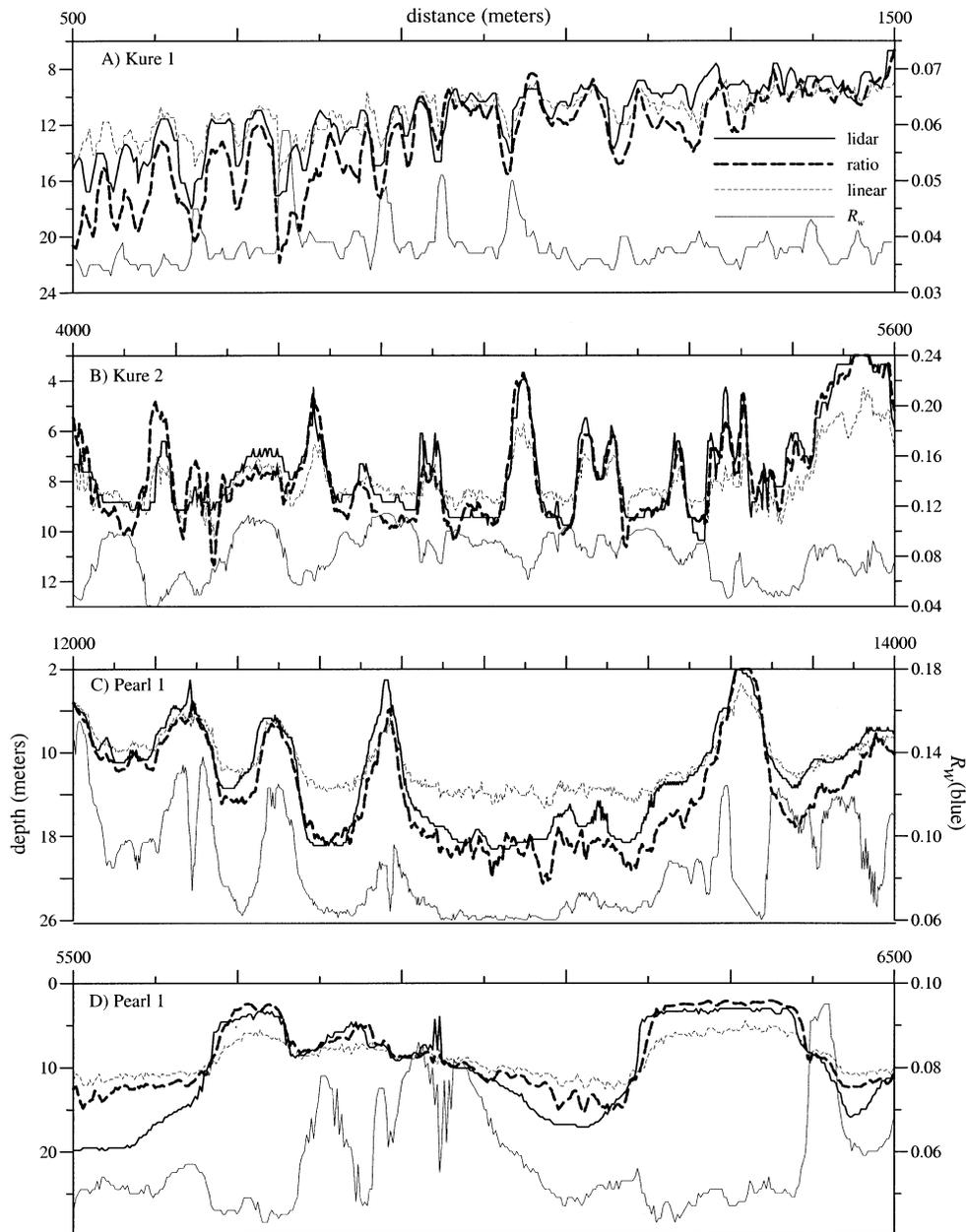
Fig. 6. Detailed profiles of depth (meters) and blue reflectance, R_w(blue). Tick marks on all graphs mark 100-m distance. (A) Kure 1: profile over spur-and-groove type structure on forereef. (B) Kure 2: profile over algae-covered pavement (former patch reefs). (C) Pearl 1: profile over coral-dominated patch and reticulated reefs. (D) Pearl 1: profile over mix of sand- and coral-dominated reefs. Note that several of the shallow areas have lower reflectance (e.g., centered near 5,700 and 6,300 m in panel D) and that the centers of the vertical reef structures at 12,300 and 13,600 m in panel C have a narrow area of low reflectance.

high-turbidity water in the basins in the southeast of the lagoon (e.g., 5,500 m in Fig. 6D), these passive methods fail, in that the true bottom cannot be detected in >15 m of water, and both algorithms generate a false bottom. This failure illustrates a fundamental limitation of depth estimation from optical systems, regardless of method.

The effectiveness of both algorithms in resolving bathymetric variations independently of variations in bottom al-

bedo is demonstrated in several areas. Shallow structures with algae and pavement are tightly resolved (Fig. 6B), and patch reefs and mini-atolls are resolved even with dramatic variations in reflectance (Fig. 6C,D) between the dark, shallow reefs and the light, typically sandy-bottom, deep basins (Fig. 7). Reef cover varies from algae-covered pavement to dense *Porites* colonies, introducing two- to fourfold variation in R_w(blue); yet, the algorithms resolve the depth vari-
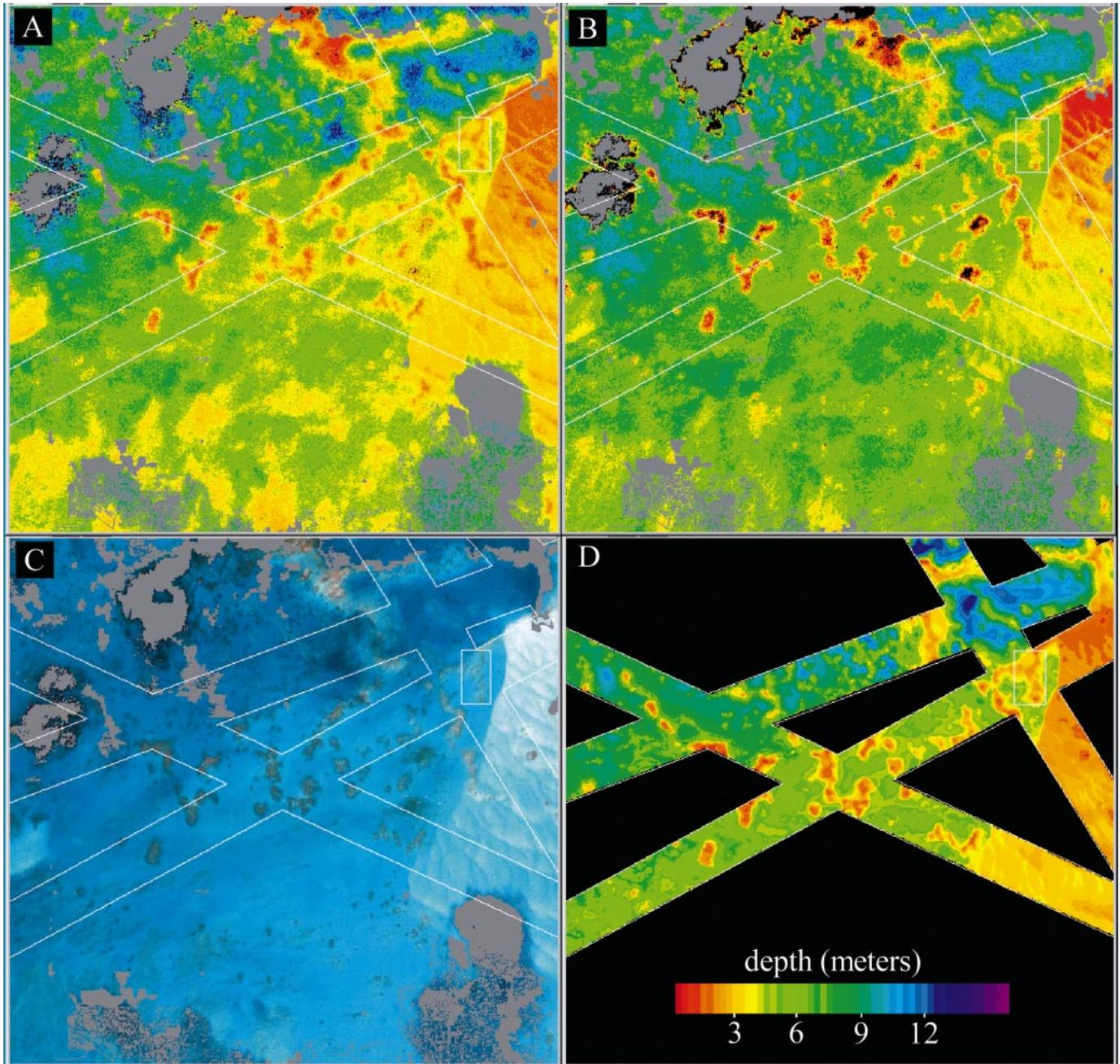
Fig. 7. Depths from the three methods and "true-color" water reflectance for central Kure: (A) ratio, (B) linear, (C) true-color, and (D) lidar. The lidar swaths are 200 m wide and marked on each image. Depths are shown in meters with scale bar at lower right. The box (at upper right in each image) marks a patch reef of low reflectance. IKONOS imagery courtesy of Space Imaging.

ations without difficulty. Shallow features can have strong variations in brightness (seen at 12,300 and 13,600 m in Fig. 6C). The most striking example is a mini-atoll in Pearl at 13,600 m in Fig. 6C, where the edges are bright and the center, which has a live bottom, is dark. In deeper water (Fig. 6A), the magnitude of the depth variation across narrow spur-and-groove types of reef structures is resolved, although there could be some constant offset from the true depth values. The sand grooves are much brighter targets than the

adjacent coral spurs but are still resolved as the deeper features they actually are.

The effectiveness of both methods in reproducing the spatial patterns in bathymetry for depths <12 m deep is exemplified in a comparison of imagery and lidar-derived depths for central Kure (Fig. 7). Several bottom types are present, as well as a large range of depths. The patch reefs located in the center are covered in dense macroalgae. Low reflectance features at top right, within the box, include alga-
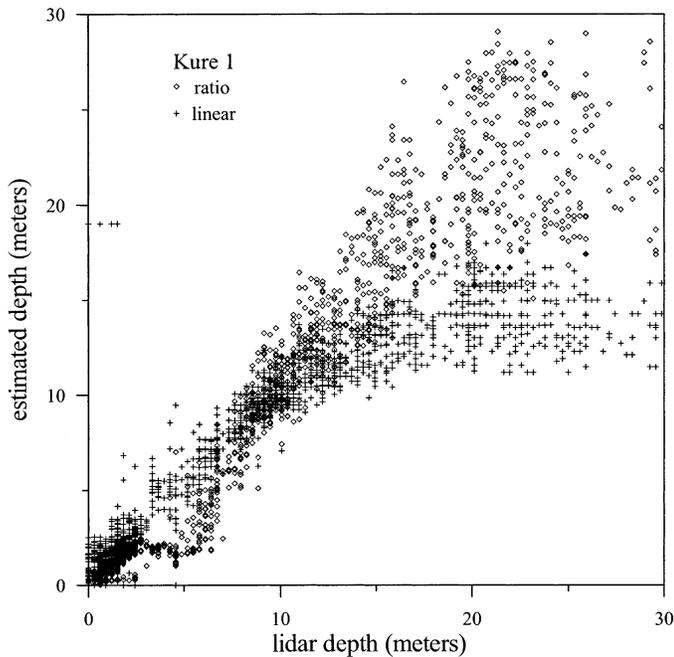
Stumpf et al.

Fig. 8. Comparison of all depths along Kure 1 (those from Fig. 4). The discrepancy in depth at 5 m occurred under a cloud shadow (*see Fig. 4*).
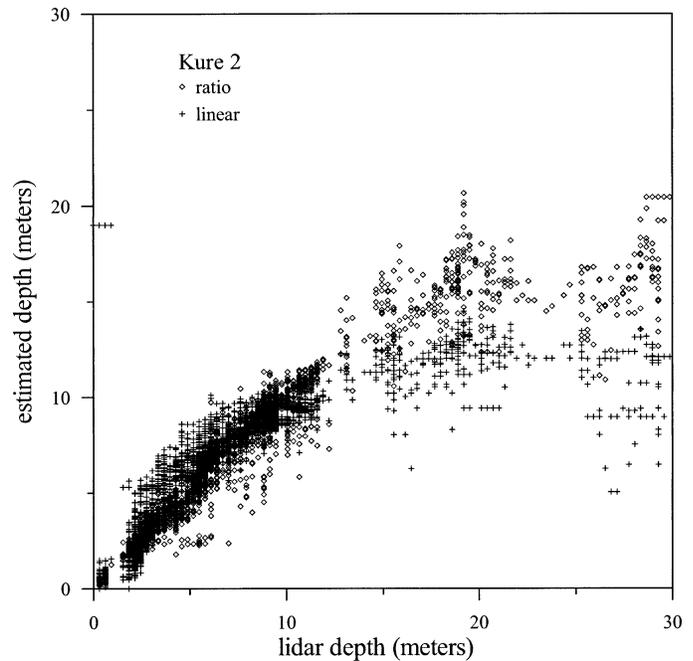

Fig. 9. Comparison of all depths along Kure 2 (those from Fig. 3). The severe discrepancy in depth in the linear algorithm from 25–30 m (derived depths < 10 m) occurred under a cloud shadow (*see Fig. 3*).

and coral-covered reefs. Elsewhere the bottom is sand, transitioning to a lower albedo carbonate pavement in the lower left. Along the right side of the image, the shallow depths are part of a large, bright, sandy region on the east side of the Kure lagoon. Both methods pick up the transition to the shallower depths, despite the much brighter reflectances, although the linear method tends to bias low relative to the actual depths. Sand waves in 2.5–4-m-deep water across the eastern side of the Kure lagoon were also resolved by both methods.

Scatterplot comparisons of the derived versus lidar depths show that both methods reproduce the depths up to 10–15 m (Figs. 8–10), with best results for the tuned transect (Fig. 9), as expected. However in depths >15 m, the linear transform rarely retrieves meaningful depths. The ratio transform provides depth information 5–10 m deeper than the linear transform. The ratio transform does have a greater amount of noise, which is not surprising since a ratio combination will inherently amplify small differences more than a linear combination and the error variability increases with depth. In the deep (lidar depths > 20 m) turbid basins of Pearl, the linear transform failed before the ratio transform (Fig. 10). Conversely, in the clear water of the deep forereef along Kure 1 (Fig. 8), depth retrievals are possible to nearly 30 m with the ratio algorithm, whereas the linear transform fails at 12–15 m.

Examining the normalized error against depth shows the difference in the effectiveness of the two methods with depth and between different transects. The ratio transform has a consistent normalized rms error of <0.3 (30%) in <25 m of water (Fig. 11). The linear transform, as expected, performs well up to 10–15 m, but the failure at that point is manifested in the increasing rms error. It is surprising that the ratio
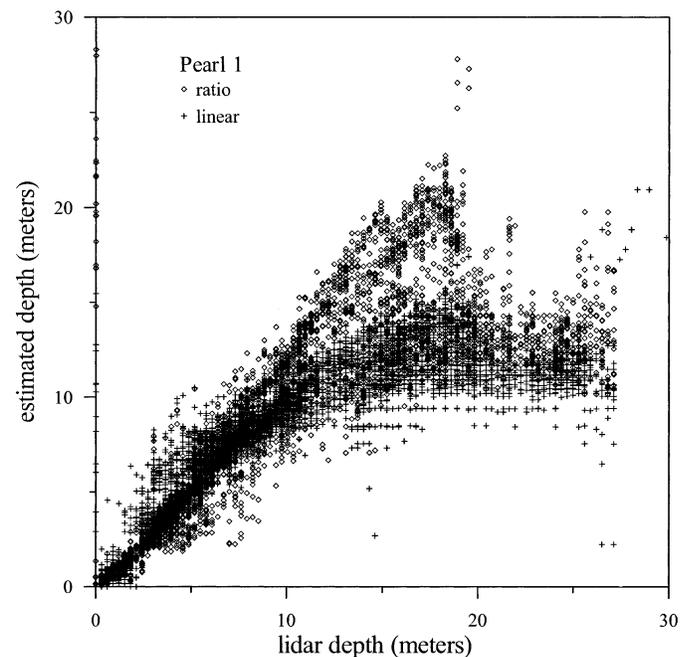

Fig. 10. Comparison of all depths along Pearl 1 (those from Fig. 5). A difference between clear and turbid areas is indicated. Areas of clear water on the forereef show consistent retrievals to 20 m with the ratio algorithm. Areas in the turbid zone of the lagoon have underestimated depths with few retrievals >15 m.
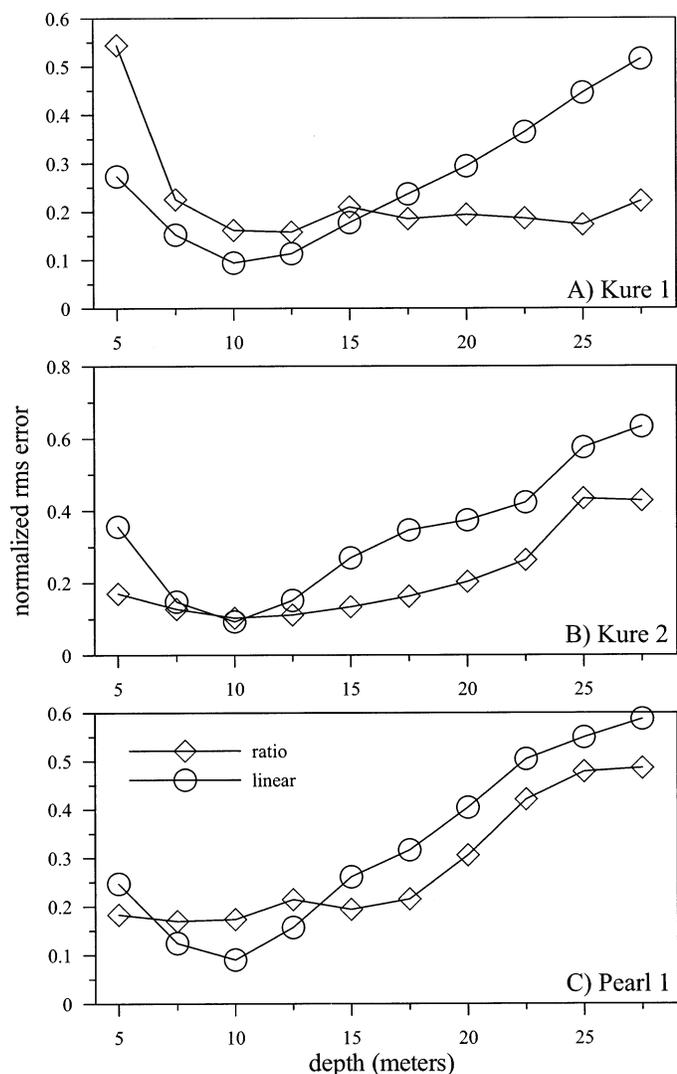
Fig. 11. Normalized root mean square (rms) error (ratio of rms error to actual depth) in 2.5-m bins for (A) Kure 1, (B) Kure 2, and (C) Pearl. The bin at 2.5 m depth was dropped because the normalization was problematic for both algorithms with water $\leq$0.6 m.

ratio transform method has fewer empirical coefficients required for the solution, which makes the method easier to use and more stable over broader geographic areas. Third, the ratio method can be tuned using available (reliable) soundings. And finally, the results shown here demonstrate that the ratio method has superior depth penetration to the linear method for a Pacific Ocean region with relatively clear water. The ratio transform has limitations relative to the linear transform, particularly in an increased level of noise.

Our first use of IKONOS imagery (Baker Island in the central Pacific) showed shallow-water areas that had lower reflectance than deep water, so the linear transform could not be implemented. Although Kure and Pearl do not have shallow-water areas that are less reflective than deep water (typically caused by extremely dense algae or seagrass cover), we have found patches of algae of $\geq$1 km^2 within the northwestern Hawaiian island chain that have a reflectance darker than deep water. Solutions for the linear transform to solve the low-albedo issue have been proposed (Van Hengel and Spitzer 1991) but require tuning of the patch as well, which only increases the number of required coefficients. The standard linear method requires five coefficients that vary with environmental conditions: $R_\infty(\lambda_i)$, $R_\infty(\lambda_j)$, a_0, a_i, and a_j, whereas the ratio method requires only two: m_0 and m_1. As a result, the ratio solution is simple to execute, since tuning can be achieved with a handful of accurate soundings. This is not a trivial issue when working in areas where few soundings are available.

The determination of R_∞ probably introduces more uncertainty in the linear algorithm than any other coefficient. With any variation in scattering, R_∞ will change in both bands, and with variations in absorption, R_∞ will change in the blue band. This is extremely difficult to determine locally and can easily vary throughout a scene. Failure to correctly determine R_∞ will affect the depth determination for deeper water. New optimization methods that have been proposed for hyperspectral instrumentation might resolve this by solving for R_∞ (Lee et al. 1999). Such methods could be useful for geographically large mapping projects when hyperspectral imagery becomes routinely available with standard processing. The ratio transform requires only bands with different water absorption and so might be applied to any sensor detecting the appropriate wavelengths.

In addition to applying the ratio transform method to more Pacific Ocean atolls, we plan to investigate ways of improving the current algorithm, in particular to examine methods for addressing moderate turbidity. The linear algorithm has an inherent solution for albedo, which must also be examined for the ratio algorithm. The simple tuning, stable results, and superior depth penetration argue for application of the ratio algorithm for mapping water depths in extensive coral reef environments similar to those found in this study.

transform performed as well as the linear transform along Kure 2 in waters <15 m depth because the linear transform was tuned to the very lidar data being used for the error evaluation, whereas the ratio transform was tuned to only a few, independent nautical chart soundings. To investigate the stability of tuning methods, the linear transform was tuned to lidar for the Kure 1 transect. This tuning produced poor results, with normalized rms errors >0.5 when applied to Kure 2.

Discussion

The ratio transform method addresses several issues that have considerable relevance to using passive multispectral imagery to map shallow-water bathymetry. First, it does not require subtraction of dark water, which expands the number of benthic habitats over which it can be applied. Second, the

References

CHAVEZ, P. S. 1996. Image-based atmospheric corrections—revisited and improved. Photogramm. Eng. Remote Sens. **62:** 1025–1035.

GORDON, H. R., D. K. CLARK, J. W. BROWN, O. B. BROWN, R. H. EVANS, AND W. W. BROENKOW. 1983. Phytoplankton pigment

concentrations in the Middle Atlantic Bight: Comparison of ship determinations and CZCS estimates. Appl. Opt. **22:** 20–36.

LEE, Z., K. L. CARDER, C. D. MOBLEY, R. G. STEWARD, AND J. S. PATCH. 1999. Hyperspectral remote sensing for shallow waters: 2. Deriving bottom depths and water properties by optimization. Appl. Opt. **38:** 3831–3843.

LUBIN, D., W. LI, P. DUSTAN, C. MAXEL, AND K. STAMNES. 2001. Spectral signatures of coral reefs: Features from space. Remote Sens. Environ. **75:** 127–137.

LYZENGA, D. R. 1978. Passive remote sensing techniques for mapping water depth and bottom features. Appl. Opt. **17:** 379–383.

———. 1981. Remote sensing of bottom reflectance and water attenuation parameters in shallow water using aircraft and Landsat data. Int. J. Remote Sens. **1:** 71–82.

———. 1985. Shallow-water bathymetry using combined lidar and passive multispectral scanner data. Int. J. Remote Sens. **6:** 115–125.

MARITORENA, S., A. MOREL, AND B. GENTILI. 1994. Diffuse reflectance of oceanic shallow waters: Influence of water depth and bottom albedo. Limnol. Oceanogr. **39:** 1689–1703.

MUMBY, P. J., C. D. CLARK, E. P. GREEN, AND A. J. EDWARDS. 1998. Benefits of water column correction and contextual editing for mapping coral reefs. Int. J. Remote Sens. **19:** 203–210.

PHILPOT, W. D. 1989. Bathymetric mapping with passive multispectral imagery. Appl. Opt. **28:** 1569–1578.

STUMPF, R. P., AND J. R. PENNOCK. 1989. Calibration of a general optical equation for remote sensing of suspended sediments in a moderately turbid estuary, J. Geophys. Res. Oceans **94:** 14,363–14,371.

VAN HENGEL, W., AND D. SPITZER. 1991. Multi-temporal water depth mapping by means of Landsat TM. Int. J. Remote Sens. **12:** 703–712.

ZHANG, M., K. CARDER, F. E. MULLER-KARGER, Z. LEE, AND D. B. GOLDGOF. 1999. Noise reduction and atmospheric correction for coastal applications of landsat thematic mapper imagery. Remote Sens. Environ. **70:** 167–180.